Hard x-ray photoemission spectroscopy of GdNi and HoNi

C. W. Chuang [1], F. M. F. de Groot [2], Y. F. Liao [1], Y. Y. Chin [3], K. D. Tsuei [1], R. Nirmala [4], D. Malterre [5], and A. Chainani [1]

[1] *National Synchrotron Radiation Research Center, Hsinchu Science Park, Hsinchu 30076, Taiwan*

[2] *Inorganic Chemistry and Catalysis, Utrecht University, Universiteitsweg 99, 3584 CG Utrecht, The Netherlands*

[3] *Department of Physics, National Chung Cheng University, Chiayi 62102, Taiwan*

[4] *Department of Physics, Indian Institute of Technology Madras, Chennai 600 036, India*

[5] *Université de Lorraine, CNRS, Institut Jean Lamour, F-54000 Nancy, France*

(Received 11 July 2020; accepted 21 September 2020; published 14 October 2020)

We study the electronic structure of GdNi and HoNi, which are magnetic materials with a Curie temperature $T_c = 69$ and $T_c = 36$ K, respectively. These materials are useful for magnetic refrigerator applications at low temperature as they exhibit a large magnetocaloric effect near T_c. We have used hard x-ray photoemission spectroscopy (HAXPES) to investigate the core-level and valence-band electronic states of GdNi and HoNi. HAXPES measurements of the Gd and Ho 3*d*, 4*d*, 4*p*, 5*p*, and 4*s* core-level spectra have been compared with atomic multiplet calculations of Gd^{3+} and Ho^{3+} ionic configurations. The good match between the experimental and calculated spectra clarify the important role of spin-orbit coupling, as well as Coulomb and exchange interactions in the intermediate-coupling scheme. The core-level spectra also show plasmons in addition to the atomic multiplets. The Gd and Ho 4*s* spectra show clear evidence of exchange splitting. The Ni 2*p* and 3*s* spectra of GdNi and HoNi show a correlation satellite at a binding energy of 7 eV above their main peaks. The Ni 2*p* and Ni 3*s* spectra could be reproduced using charge transfer multiplet calculations. Valence-band HAXPES of GdNi and HoNi shows that the Gd 4*f* and Ho 4*f* features are also consistent with atomic multiplets and occur at high binding energies away from the Fermi level. The Ni 3*d* density of states are spread from the Fermi level to about 3 eV binding energy. The results indicate a partially filled Ni 3*d* band and show that the charge transfer model is not valid for describing the electronic structure of GdNi and HoNi.

DOI: 10.1103/PhysRevB.102.165127

I. INTRODUCTION

There is a growing interest in rare-earth and transition-metal based intermetallic alloys for magnetic refrigeration applications [1–4]. Since most rare-earth 4*f* electrons in intermetallic alloys usually behave like localized electrons, they often exhibit a large magnetic moment. The localized 4*f* magnetism is essentially characterized by the magnetic exchange interaction, magnetic anisotropy, and crystal-field effects, which often dominate the magnetic and transport properties of rare-earth intermetallic alloys. This gives rise to exotic phenomena such as giant magnetoresistance, large magnetocaloric effect, and colossal magnetostriction in some of these materials [3–7]. On the other hand, transition-metal *d* electrons can be localized or delocalized depending on the crystal structure and their electron configuration [8]. Thus, the interplay of rare-earth and transition-metal magnetism and the associated transport properties continue to be important topics for basic and applied research [3,4].

It is well established that in intermetallics consisting of rare earths and transition metals, most rare-earth atoms normally exhibit trivalent ground states, except for Ce, Eu, Sm, and Yb which can show mixed valency [5–7]. The trivalency also usually means that the rare-earth ions show nearly full local moments. However, when the concentration of the rare earth in such alloys is increased relative to the transition-metal content, the magnetic moments of the transition-metal sites get reduced [5]. This is based on the fact that the transition-metal 3*d* band gets gradually filled on increasing rare-earth content in the alloy. This model is called the charge transfer model and it could successfully explain the properties of a large number of intermetallic compounds in the series *RM*, R_xM_{1-x}, RM_2, etc. (*R*: rare earth; *M*: typically late transition metals, such as Fe, Co, Ni, Cu) [5–7]. But there are some known exceptions to this model, such as the alloy system Gd_xFe_{1-x} with $0.1 \leqslant x \leqslant 0.4$ [9], GdNi [10,11], $GdNi_2$ [12], etc. This leads us to some questions in relation to such intermetallic alloys consisting of rare-earth and transition-metal elements: What are their effective valencies? What are their element-specific magnetic properties? What is the relation of the rare-earth and transition-metal states with their properties? We address these questions from a comparative study of the electronic structure of GdNi and HoNi using hard x-ray photoemission spectroscopy (HAXPES).

The crystal structures of GdNi and HoNi are both orthorhombic, but with small differences. GdNi has the *CrB*-type structure, with space group *CmCm*, No. 63, while HoNi has the *FeB*-type structure, with space group *Pnma*, No. 62 [13–15]. The basic structural motif is a trigonal prism for both GdNi and HoNi, with the Ni atoms positioned at the center of the prism and the rare-earth atoms occupying the corners of the prism. GdNi exhibits a ferrimagnetic transition at

$T_c = 69$ K [10,11,13–16], while HoNi shows a ferromagnetic transition at $T_c = 36$ K with an additional spin-reorientation transition within the magnetically ordered state [13–15,17]. Magnetic studies have inferred that the Gd and Ho sites are both trivalent with a $4f^7$ and $4f^{10}$ configuration, respectively. While the Gd^{3+} state in GdNi has been confirmed by x-ray absorption spectroscopy (XAS) [10,11], there is no XAS study of HoNi reported to date. Electrical resistivity studies have shown that both GdNi and HoNi are metallic materials which show a clear knee-point at their magnetic transitions with a reduced resistivity in the magnetically ordered phases. While the resistivity measured on single-crystal GdNi and HoNi below T_c was attributed to magnetic disorder scattering typical of ferromagnets, the resistivity above T_c was linear at least up to room temperature for GdNi and HoNi [16,17]. In general, a linear resistivity for $T > \Theta_D$ (Debye temperature) is typical of many metals and attributed to scattering of conduction electrons by phonons. However, the estimated Θ_D from specific-heat measurements for GdNi and HoNi are $\Theta_D \sim 130$ K [18] and ~200 K [19], respectively. Thus, a linear resistivity just above T_c and significantly below Θ_D is rather unusual and suggestive of non-Fermi-liquid behavior. It is also noted that the specific-heat coefficient $\gamma = 45$ mJ/mol K^2 for GdNi [18]. For HoNi, the estimation of γ was not easy as the specific heat shows an upturn at the lowest temperature [19]. However, the authors used LuNi as a reference nonmagnetic system and estimated $\gamma = 2.7$ mJ/mol K^2 for HoNi, but this seems to be too low when compared to the value obtained for GdNi.

Early studies of the magnetic moment of Ni in GdNi suggested that Ni is nonmagnetic, assuming that the Ni $3d$ shell was fully occupied by electrons donated by forming the Gd^{3+} state [20,21]. This would have made it consistent with the charge transfer model discussed above. However, subsequent XAS and x-ray magnetic circular dichroism (XMCD) studies indicated a small finite magnetic moment for Ni, antiferromagnetically aligned to the Gd magnetic moment [10]. The spin magnetic moment for Ni was estimated to be $m_s = 0.09$ μ_B and the orbital magnetic moment was $m_o = 0.014$ μ_B, but the Gd magnetic moment was not quantified. However, another magnetic study concluded that the Gd moment was ferromagnetically aligned with Ni moments, effectively leading to an excess moment of 7.2 μB compared to the expected theoretical value of a saturation moment of 7 μB for an isolated Gd trivalent ion [22]. Based on band structure calculations, it was shown by Paudyal *et al.* [23] that Gd can have a $4f$ spin magnetic moment of 7 μ_B in GdNi, with Gd $5d$ electrons also showing a finite moment of 0.3 μ_B, and Ni $3d$ electrons showing a moment -0.1 μ_B. This confirmed that the Gd moment is antiferromagnetically aligned with Ni moments in GdNi, as shown earlier by experiments. In a recent study using XAS and XMCD experiments combined with a sum-rule analysis and model calculations [11], it was shown that the Gd ions exhibit a spin magnetic moment $m_s = 6.42 \pm 0.1$ μ_B; that is, it is slightly reduced compared to the 7 μ_B expected from the $S = 7/2$ ground state, and a small orbital magnetic moment for Gd ions, $m_o = 0.032 \pm 0.01$ μ_B, was reported. The Ni ions showed consistent values with the earlier study [10], with a small spin magnetic moment, $m_s = 0.11 \pm 0.01$ μ_B, and an orbital magnetic moment, $m_o = 0.012 \pm 0.01$ μ_B, giving $m_{tot} = 0.12 \pm 0.02$ μ_B.

Neutron-diffraction experiments have shown that GdNi exhibits a collinear arrangement of Gd magnetic moments [14,24], while HoNi shows a noncollinear magnetic structure of Ho magnetic moments [25–27]. The Ho moments are ferromagnetic along the a axis and antiferromagnetic along the c axis [25–27]. Magnetic studies have shown that the Ho saturation moment is 9.2 μ_B/formula unit, and this is less than the value expected for the full moment of a Ho^{3+} ion, i.e., 10.4 μ_B/formula unit. The reduced moments might be due to a partial quenching of the orbital angular momentum of Ho^{3+} ions in the crystalline electric field of neighboring Ni ions, or may be due to a strong magnetic anisotropy [28]. Paudyal *et al.* also showed that the anisotropic shifts in lattice constants are responsible for a large spontaneous linear magnetostriction effect of 8000 ppm along the c direction and GdNi can be classified as a giant magnetostriction compound [23], which would favor a strong magnetic anisotropy.

Surprisingly, there are no core-level and valence-band photoemission spectroscopy studies of GdNi and HoNi reported to date, except for a recent study in which we reported the valence-band spectrum of GdNi along with the XAS and XMCD results [11]. In the present study, we have carried out a comparison of bulk sensitive HAXPES [29,30] of the core level and valence band of HoNi with GdNi to characterize their intrinsic electronic structure. HAXPES of Gd and Ho $3d$, $4d$, $4p$, and $5p$ core-level spectra were measured and analyzed using atomic multiplet calculations [31–33], which confirm the Gd^{3+} and Ho^{3+} ionic configurations in GdNi and HoNi, respectively. The results show that spin-orbit interactions and core-valence electrostatic interactions in the intermediate-coupling scheme are necessary to explain the spectra. The Gd and Ho $4s$ spectra show clear evidence of exchange splitting, confirming the local moments of Gd and Ho. The Ni $2p$ and $3s$ spectra of GdNi and HoNi show a Coulomb correlation satellite. Valence-band HAXPES of GdNi and HoNi show that the Gd $4f$ and Ho $4f$ features are also consistent with atomic multiplet calculations and occur at high binding energies away from the Fermi level. The Ni $3d$ density of states (DOS) indicate a partially filled Ni $3d$ band in HoNi, quite similar to that observed in GdNi, thus confirming that the charge transfer model indeed does not hold good for heavy rare-earth containing RNi compounds.

II. METHODS

GdNi and HoNi polycrystalline samples were synthesized using the arc-melting method [34,35]. The high-purity constituent elements were melted in an argon atmosphere, followed by an annealing process for 12 hours at $T = 1173$ K. Powder x-ray diffraction measurements were employed to confirm the phase purity of the samples. Magnetization measurements using a physical property measurement system (PPMS) were carried out to confirm the magnetic transitions in GdNi and HoNi. The ferrimagnetic transition temperature of GdNi was confirmed to be $T_c = 69$ K and the ferromagnetic transition in HoNi was confirmed to be $T_c = 36$ K, respectively. The changes in magnetization associated with

the spin-reorientation transition which occurs at $T = 15$ K in HoNi was also observed in the data, as reported in earlier studies [25–27,34,35]. HAXPES was used to measure the core levels and valence band of GdNi and HoNi. The HAXPES measurements were carried out at the Taiwan beam line BL12XU in SPring-8, Hyogo, Japan using linearly polarized radiation and a photon energy $h\nu = 6500$ eV. A liquid N_2 flow cryostat was used to cool the sample down to $T = 80$ K. The Fermi edge (E_F) of gold thin film was measured at $T = 80$ K to obtain the energy resolution and to calibrate the binding-energy (BE) scale. The estimated total-energy resolution of HAXPES is 0.255 eV, obtained by fitting the Fermi edge of gold. The GdNi and HoNi polycrystals were cleaved in an ultrahigh vacuum preparation chamber at 5×10^{-9} mbar, and immediately transferred to the main chamber at 8×10^{-10} for the measurements.

The Gd and Ho $3d$, $4d$, $4p$, $5p$, and $4s$ core-level spectra were simulated using atomic multiplet calculations using the QUANTY code [31–33]. The parameters of the atomic multiplet calculations are listed in the Appendix, Tables V–XV. The photoemission spectrum is calculated as the creation of a core hole in the initial state going to a final state with a free photoemitted electron. For example, the $3d$ spectrum of Gd is calculated as the $3d^{10}4f^7$ initial state going to the final state $3d^9 4f^7$ + one free photoemitted electron. We did not need to include ligand screened excited-state configurations, such as $3d^9 4f^8 \underline{L}^1$ (where $\underline{L}^1$ corresponds to a hole in the ligand states), for the Gd $3d$ photoemission calculations. For comparison with experimental spectra, we employed an energy-dependent Lorentzian broadening convoluted with a Gaussian, and an integral background was added to the calculated spectra. For the Ni $3s$ and Ni $2p$ cases, the charge transfer multiplet (CTM) program [36], which includes atomic multiplets and charge transferred states, was used to calculate the spectra. It is noted that the charge transfer model [5–7], discussed in Sec. I in relation to the filling of the transition-metal d band by the electrons donated by the rare-earth atoms, is distinct from the CTM program used to calculate the Ni $3s$ and Ni $2p$ spectra. More specifically, as will be shown in the following, the rare-earth spectra of Gd and Ho are best explained by Gd^{3+} and Ho^{3+} electron configurations, i.e., $4f^7$ and $4f^{10}$, respectively. The charge transfer model was developed to discuss the role of the donated electrons by the rare earth (Gd and Ho, in the present case) to the nearest-neighbor transition metal (Ni, in the present case) in terms of a qualitative analysis for describing the phenomenology [5–7,9–12]. If the electrons were transferred to the Ni site, it can be expected to fill the Ni $3d$ band and then the Ni would not exhibit a magnetic moment. If the Ni sites exhibit a magnetic moment, it indicates that the Ni $3d$ band is not fully occupied and the electrons are donated to the delocalized conduction band [10–12]. On the other hand, while we can simulate the Gd or Ho spectra using a purely atomic model, we needed to carry out CTM calculations for simulating the Ni $3s$ and $2p$ spectra. The CTM calculations use a mixture of d^n and $d^{n+1}\underline{L}^1$ states (in the present case for Ni, we have used d^8 and $d^9\underline{L}^1$), where $\underline{L}^1$ represents a symmetry-adapted ligand hole state, to describe the initial and final states. The term "charge transfer" in the CTM calculation corresponds to the electron transferred from the ligand (L) site to the transition-metal d site, resulting in a $d^{n+1}\underline{L}^1$ state. The initial state and final states can then be described as a linear combination of the d^n and $d^{n+1}\underline{L}^1$ states. Thus, the meaning of charge transfer in the charge transfer model and in the CTM calculations is very different. The parameters of the charge transfer multiplet calculations are listed in the Appendix, Tables XVI–XIX. For the interested reader, further details of the calculation method are described in Refs. [36–38]. Finally, a least-squares method was used to fit the Gd and Ho $3d$, $4s$ as well as the Ni $3s$ and $2p$ core-level spectra of GdNi and HoNi in order to quantify peak-energy positions and widths. The spectra were fitted using a Shirley-type background with asymmetric Doniach-Sunjic (DS)-type Voigt profiles for the main peaks, and symmetric Gaussians for the satellites and plasmons.

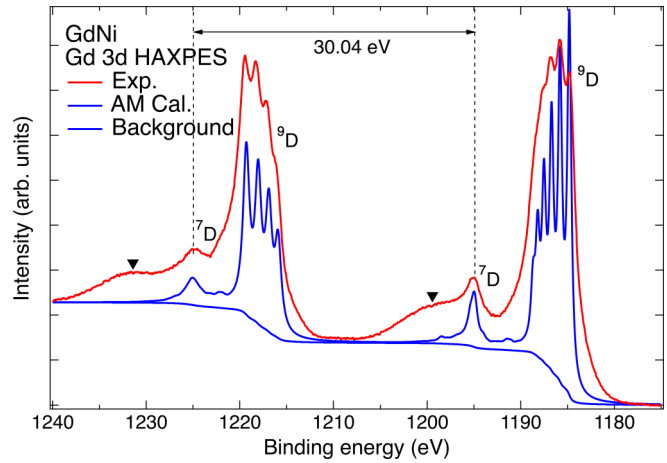

FIG. 1. The Gd $3d$ core-level HAXPES spectrum measured at $T = 80$ K compared with the atomic multiplet (AM) calculated spectrum. The inverted triangles mark the plasmon features in GdNi.

III. RESULTS AND DISCUSSIONS

Figure 1 shows the Gd $3d$ core-level HAXPES spectrum of GdNi measured at $T = 80$ K. The Gd $3d$ core-level spectrum consists of two regions of rich spectral features spread over several electron volts (eV), which can be assigned to spin-orbit-coupling derived $3d_{5/2}$ and $3d_{3/2}$ states. The main broad peak of the $3d_{5/2}$ and $3d_{3/2}$ states consists of several multiplets. In order to understand the atomic multiplets of the Gd $3d$ spectrum, we carried out atomic multiplet calculations for Gd^{3+} ions using the QUANTY code [31–33], as described in Sec. II. The obtained results, plotted together with the experimental spectrum in Fig. 1, confirm that Gd ions are trivalent. The calculated spectrum allows us to characterize all the $3d_{5/2}$ and $3d_{3/2}$ atomic multiplet peaks. In the calculated spectrum, the $3d_{5/2}$ main broad peak consists of six subpeaks assigned to the ^9D states, and a lower-intensity peak at higher BE of 1194.97 eV, which is assigned to the ^7D states [39]. In addition, there are two small features at BEs of 1191.42 and 1198.53 eV for the $3d_{5/2}$ states. The $3d_{3/2}$ main broad peak consists of four subpeaks, which are again due to the ^9D states and the lower-intensity peak at a BE of 1225.01 eV is due to the ^7D states. The spin-orbit splitting is measured to be 30.04 eV in terms of the energy separation of the ^7D peak of the $3d_{5/2}$ (positioned at 1194.97 eV) and $3d_{3/2}$ (positioned at

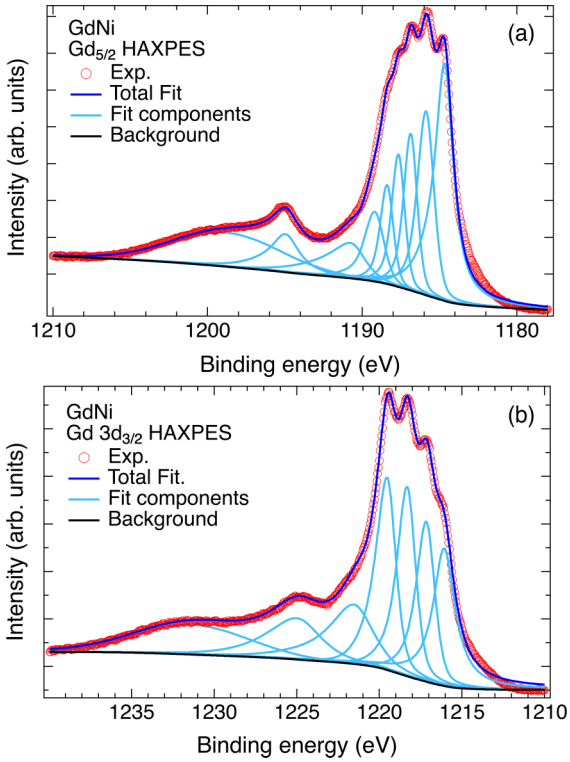

FIG. 2. The fitting results of the Gd $3d$ HAXPES spectrum obtained by using a least-squares method for (a) the Gd $3d_{5/2}$ states and (b) the Gd $3d_{3/2}$ states. The fitting parameters are listed in Table I.

TABLE I. Fitting parameters for the Gd $3d$ core-level spectra, with component peaks listed from lowest binding energy to highest binding energy.

Component peaks Gd $3d_{5/2}$	Fitted peaks (FWHM) (eV)	Atomic multiplet calc. peaks (eV)	Difference (eV)
1 ($J'=6$)	1184.96 (1.47)	1184.8	0.16
2 ($J'=5$)	1185.88 (1.27)	1185.8	0.08
3 ($J'=4$)	1186.87 (1.04)	1186.7	0.17
4 ($J'=3$)	1187.66 (1.01)	1187.52	0.14
5 ($J'=2$)	1188.40 (1.00)	1188.19	0.11
6 ($J'=1$)	1189.19 (1.51)	1188.69	0.5
7	1190.78 (3.06)	1191.42	−0.64
8 (^7D)	1194.97 (2.33)	1195.06	0.09
Plasmon	1198.79 (8.23)		
Gd $3d_{3/2}$	(eV)	(eV)	(eV)
1 ($J'=2$)	1216.08 (1.59)	1216.2	−0.12
2 ($J'=3$)	1217.17 (1.35)	1217.2	−0.03
3 ($J'=4$)	1218.33 (1.35)	1218.4	−0.07
4 ($J'=5$)	1219.54 (1.47)	1219.5	0.04
5	1221.56 (3.21)	1222.17	−0.61
6 (^7D)	1225.01 (3.89)	1225.1	−0.09
Plasmon	1231.38 (8.00)		

1225.01 eV) states, as marked in Fig. 1. Two very weak small features at BEs of 1222.17 and 1226.97 eV are also seen in the spectrum. While the calculated spectrum matches fairly well with the experimental spectrum, there are discrepancies in the form of additional weak-intensity broad features centered at BEs of ∼1200 and ∼1232 eV (labeled with inverted triangles in Fig. 1), which are not observed in the calculated spectrum. As confirmed by measurements of other core levels, these two broad peaks are assigned to the plasmons associated with the multiplets of the main broad peaks. Although there are six multiplets in the main $3d_{5/2}$ and four in the $3d_{3/2}$ peak in the calculated spectrum, the plasmons of the multiplets get merged together and show up as a single broad feature. In order to quantitatively check the various atomic multiplet features and the plasmon energy position, we carried out a least-squares-method fitting of the Gd $3d_{5/2}$ and $3d_{3/2}$ states, as discussed in the following.

The results of the least-squares fit for the Gd $3d_{5/2}$ and $3d_{3/2}$ states with peak energies as free parameters are shown in Figs. 2(a) and 2(b), respectively. The fitted peak positions are compared with peak positions obtained from atomic multiplet calculations as shown in Table I. It is noted that if the LS coupling scheme was correct, the ^9D states of Gd $3d_{5/2}$ and Gd $3d_{3/2}$ main peaks would have five multiplets each, with $J'=6$, 5, 4, 3, 2. The least-squares fitting of the Gd $3d$ spectra thus also allows us to distinguish LS coupling from jJ coupling. As seen in Table I, the energies of all the fitted features are within ±0.2 eV compared to the atomic multiplet calculations, except for peaks 6 and 7 in the Gd $3d_{5/2}$ fit and peak 5 in the in Gd $3d_{3/2}$ fit, which differ by ∼0.5 to ∼0.6 eV. However, it is clear from the fitting results that the $3d_{5/2}$ main peak consists of six peaks, which is consistent with the jJ coupling scheme: the $4f^7$ valence angular momentum $J=7/2$ couples with the $3d$ core-hole angular momentum $j=5/2$, resulting in the the total angular momentum $J'=6$, 5, 4, 3, 2, 1 multiplets. The six multiplets $J'=6$, 5, 4, 3, 2, 1 can be said to correspond to what would have been the ^9D states of the LS coupling scheme, with the core-hole coupling with the ^8S parent term of the $4f^7$ configuration. They show narrow broadening and the lowest BE corresponds to the $J'=6$ final state, with the spin and orbital moments of the $3d$ level and the spin moment of the $4f$ shell all parallel to each other [39]. On the other hand, the single peak at a BE of 1194.97 eV is due to LS coupling: the $3d^9$ (^2D) state with a spin-up core hole couples with the $4f^7$ (^8S) state, resulting in the ^7D states with a higher BE compared to the ^9D state at lower BE. Since the ^7D state can also be formed by coupling with higher-energy terms ^6P, ^6D, ^6F, ^6G of $4f^7$, it results in a single broad peak with a large lifetime broadening. In addition, since we obtained a small feature at a BE of 1191.42 eV in the atomic multiplet calculated spectrum shown in Fig. 1, we needed to include this extra peak in the $3d_{5/2}$ peak fitting to obtain the best fit with experiment.

From the fitting results of the $3d_{5/2}$ peak listed in Table I, we can know the position of the six multiplets in the ^9D state: the energy separation between each of the six multiplets is ∼1 eV and the ^7D state is at BE of 1194.97 eV, which is 10.01 eV BE higher than the multiplet peak $J'=6$. The plasmon is marked at a position of ∼14 eV BE higher than the multiplet peak $J'=6$. Similarly, for the $3d_{3/2}$ peak fitting results shown in Fig. 2(b), the $3d_{3/2}$ main peak consists of four peaks, and the separations between these peaks are roughly around 1.1 eV. These four multiplet peaks are due to jJ

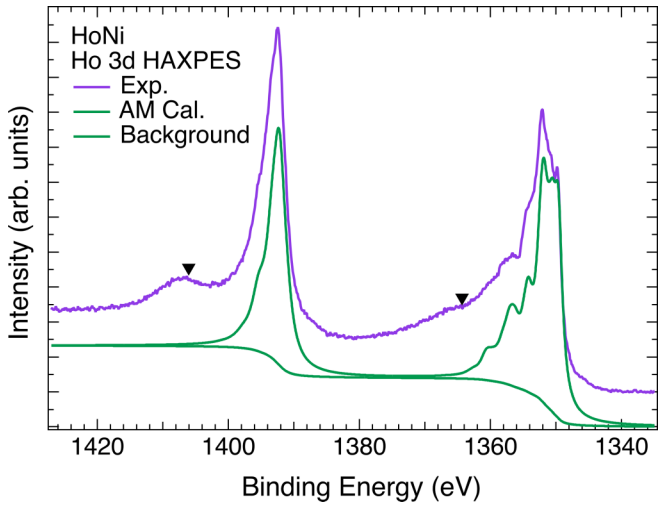

FIG. 3. The Ho 3*d* core-level HAXPES spectrum measured at $T = 80$ K compared with atomic multiplet (AM) calculations.

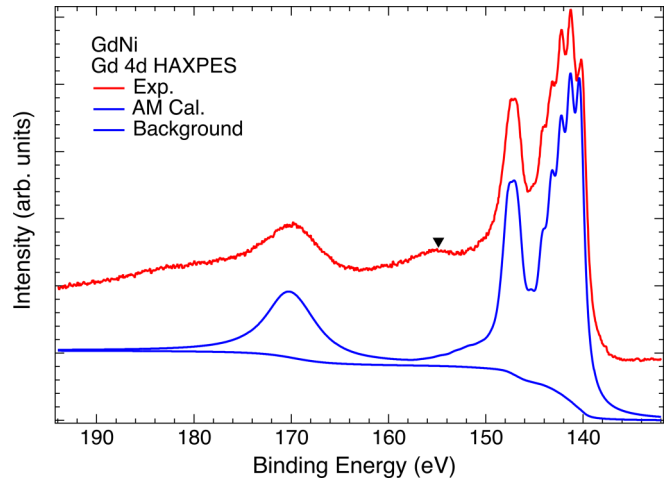

FIG. 4. The comparison of experimental Gd 4*d* core-level HAXPES of GdNi measured at $T = 80$ K with atomic multiplet (AM) calculations.

coupling: the 3*d* core-hole angular momentum $j = 3/2$ couples with the $4f^7$ valence angular momentum $J = 7/2$, resulting in total angular momentum $J' = 5, 4, 3, 2$ multiplets. Here, the $J' = 2$ is the lowest BE state because the spin moment of the 4*f* shell and the spin moment of the 3*d* core are parallel to each other, but they are aligned antiparallel to the 3*d* orbital angular momentum [39]. This corresponds to an opposite ordering sequence compared to the ordering of the six multiplets of $3d_{5/2}$ states, for which the lowest BE state is $J' = 6$. And again, the broad single peak at BE of 1225.01 eV is the ^7D state due to the *LS* coupling. The plasmon peak is at a BE of 1231.38 eV, which is about 15.30 eV higher BE than the $J' = 2$ multiplet peak. In addition, since we obtained a small feature at a BE of 1222.17 eV in the atomic multiplet calculated spectrum shown in Fig. 1, we needed to include this extra peak in the $3d_{3/2}$ peak fitting to obtain the best fit with experiment. A similar analysis in terms of the intermediate-coupling scheme invoking *jJ* coupling for the multiplets within the main peak (^9D states) and *LS* coupling for the low-intensity feature at about 10 eV higher BE was reported for the Gd $3d_{5/2}$ and $3d_{3/2}$ states of amorphous GdFe films [39].

In Fig. 3, we plot the Ho 3*d* core-level HAXPES spectrum of HoNi measured at $T = 80$ K. The spectrum consists of two main broad spin-orbit split $3d_{5/2}$ and $3d_{3/2}$ features consisting of multiple peaks. The highest-intensity feature of the $3d_{5/2}$ states is positioned at a BE of 1352.15 eV, while that for the $3d_{3/2}$ peak is at a BE of 1392.60 eV. The separation between these spin-orbit split features is 40.45 eV. The $3d_{5/2}$ states contain many multiplet peaks, and while it is not clear for the $3d_{3/2}$ peak, they also consist of several multiplet peaks. We confirmed this by carrying out atomic multiplet calculations of Ho^{3+} ions for Ho 3*d* spectra. The good match of the calculated spectrum with the experimental spectrum as shown in Fig. 3 confirms Ho ions are trivalent in HoNi. Following the same method as for Gd $3d_{5/2}$ and $3d_{3/2}$ peaks, in the *jJ* coupling scheme, the Ho $3d_{5/2}$ and $3d_{3/2}$ states also consist of six peaks and four peaks, respectively. The $3d_{5/2}$ core-hole angular momentum $j = 5/2$ couples with the $4f^{10}$ valence angular momentum $J = 8$, resulting in six multiplet peaks with total angular momentum $J' = 21/2, 19/2, 17/2, 15/2, 13/2, 11/2$. On the other hand, for the $3d_{3/2}$ core-hole angular momentum $j = 3/2$ coupling with the $4f^{10}$ states, it results in four multiplets with total angular momentum $J' = 19/2, 17/2, 15/2, 13/2$. However, for HoNi also, the experimental spectrum has two additional weak broad features at BEs of 1365.10 and 1407.80 eV. These two additional peaks in the experimental spectrum are assigned to the plasmons of HoNi at a BE of roughly 15.20 eV from the main peak, based on the fact that other core-level spectra of HoNi also show similar features, as discussed later.

The Gd 4*d* core-level HAXPES spectrum of GdNi measured at $T = 80$ K is shown in Fig. 4. We can observe many atomic multiplets in the Gd 4*d* HAXPES spectrum compared to the multiplets in the Gd 3*d* spectrum, suggesting that the Gd 4*d* spectrum is more complicated. The experimental spectrum is compared with atomic multiplet calculations to understand the Gd 4*d* core-level spectral features, as shown in Fig. 4. The calculated spectrum matches fairly well with the experimental spectrum. Our experimental and calculated spectra are consistent with earlier studies on Gd metal and Gd intermetallic compounds [40–44]. It was shown in these earlier studies that an intermediate-coupling scheme between the *LS* coupling and *jJ* coupling was appropriate for describing the Gd 4*d* spectrum of Gd metal. We follow the same analysis for explaining the Gd 4*d* spectrum of GdNi. First, we use the *LS* coupling scheme to explain that the core-hole $4d^9$ (^2D) state couples with the valence $4f^7$ (^8S) state, resulting in the ^7D and ^9D final states. The ^9D states have lower BE and will get split into five levels given by $J = 6, 5, 4, 3, 2$ due to the small spin-orbit coupling. As we can see in Fig. 4, the ^9D states in the experimental and calculation spectra correspond to an envelope of the Gd 4*d* states within the BE range from 138 to 145 eV, consisting of five peaks. Similarly, the small spin-orbit coupling will split the ^7D states into five levels $J = 5, 4, 3, 2, 1$. However, the ^7D states are not only formed by coupling with the ^8S terms of $4f^7$, but they can also be formed by coupling with the higher-energy terms ^6P, ^6D, ^6F,

^6G of $4f^7$. The Coulomb and exchange interaction between these ^7D states destroys the regular five-peak splitting pattern of $J = 5, 4, 3, 2, 1$ of ^7D. Thus, the most intense narrow lowest-energy $^7D_1$ states at BE of 147.21 eV and the lower-intensity highest-energy $^7D_5$ states at the BE of 170.21 eV are obtained. Three more ^7D states are expected at energies between 147.21 and 170.21 eV, but they are not observed due to very low relative intensities of less than 0.1%, as was shown in the case of Gd metal [42]. The energy separation between the lowest BE peak of the ^9D states and the most intense ^7D states, and that with the highest-energy ^7D states, is 7 and 30 eV, respectively. However, there is a weak broad feature at a BE of 154.81 eV in the experimental spectrum, which is not obtained in the calculated spectrum. This is assigned to the plasmon peak of GdNi based on an energy separation of ∼14.6 eV from the lowest BE multiplet. This is consistent with the plasmons seen in the Gd $3d$ (Fig. 1), $4p$ (Fig. 4), and $4s$ (Fig. 8) states.

Figure 5 shows the Ho $4d$ core-level HAXPES spectrum of HoNi measured at $T = 80$ K. We can observe two sharp and high-intensity peaks at low BEs of 159.41 and 161.51 eV. The separation between the two sharp peaks is 2.10 eV, and there are some small features at BEs of 163.61, 165.31, and 167.90 eV. On the other hand, there are two broad peaks at high BE of 175.66 and 188.96 eV. Similar spectra were reported for the compounds $HoRhB_3$ [45] and HoB_4 [46], but the spectral features were not analyzed in terms of atomic multiplets. The Ho $4d$ spectrum compared with atomic multiplet calculations is shown in Fig. 5 and the calculated spectrum matches well with the experimental spectrum. The calculated spectrum is also consistent with early studies of Ho $4d$ atomic multiplet calculations, which were compared with a Ho metal photoemission spectrum [41]. The atomic multiplets in Ho $4d$ can be explained by the LS coupling scheme, just like we analyzed for the Gd $4d$ spectrum. From the LS coupling scheme, the $4d^9(^2D)$ states coupling with $4f^{10}(^5I)$ states will result in 10 states: ^6L, ^6K, ^6I, ^6H, ^6G, ^4L, ^4K, ^4I, ^4H, ^4G. It is noted that since we have high BE multiplet peaks in the Ho $4d$ spectrum, it is not easy to observe the plasmons in Ho $4d$. The plasmons are probably hidden inside the broad peak at high BE of 175.66 eV.

The Gd $4p$ core-level HAXPES spectrum of GdNi measured at $T = 80$ K is plotted in Fig. 6(a). The spectrum consists of the main $4p_{3/2}$ peak at a BE of 271.5 eV and the main $4p_{1/2}$ peak at 309.4 eV, both with many $4p^54f^7$ multiplet features at higher binding energies. The measured Gd $4p$ spectrum is similar to that of Gd metal obtained using soft x-ray PES that has been interpreted in terms of atomic multiplets [43,47,48]; we have repeated these calculations for the Gd $4p$ spectrum as shown in Fig. 6(a) along with the experiment. The calculated spectrum shows several multiplet features spread in two energy ranges of BEs, between 269.5 and 286.6 eV and between 306.6 and 315 eV. While the main peak at the BE of 271.46 eV and the second-highest-intensity feature at a BE of 310.07 eV match well with the experiment, the weaker-intensity features show some discrepancy with experiment. The main reason for the discrepancies is the configuration-interaction (CI) effect between the $4p^54f^7$ configuration and the $4d^84f^8$ configuration. This is a special phenomenon happening specifically for the rare-earth $4p$ core

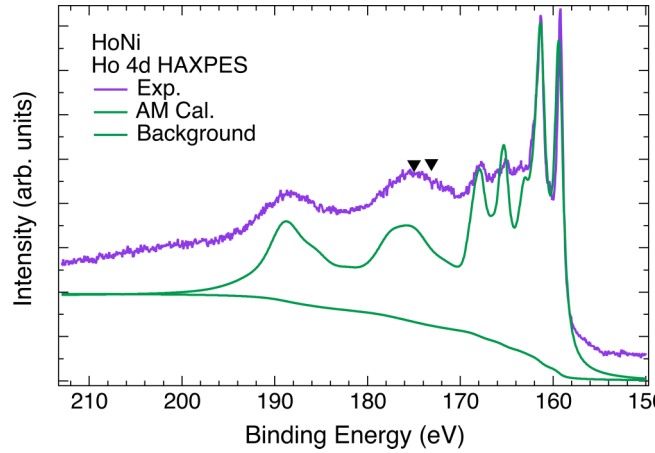

FIG. 5. The Ho $4d$ HAXPES spectrum of HoNi measured at $T = 80$ K compared with atomic multiplet (AM) calculations.

levels and this effect is strong because the binding energy of the $4p$ state is approximately twice that of the $4d$ state, thereby yielding strong CI between the configurations. Calculations including this CI effect have been performed for Gd metal by Tagliaferri *et al.* [49]. In the $4p$ HAXPES spectrum, the main discrepancy between the atomic multiplets and the experiment is caused by the CI effects that are stronger than

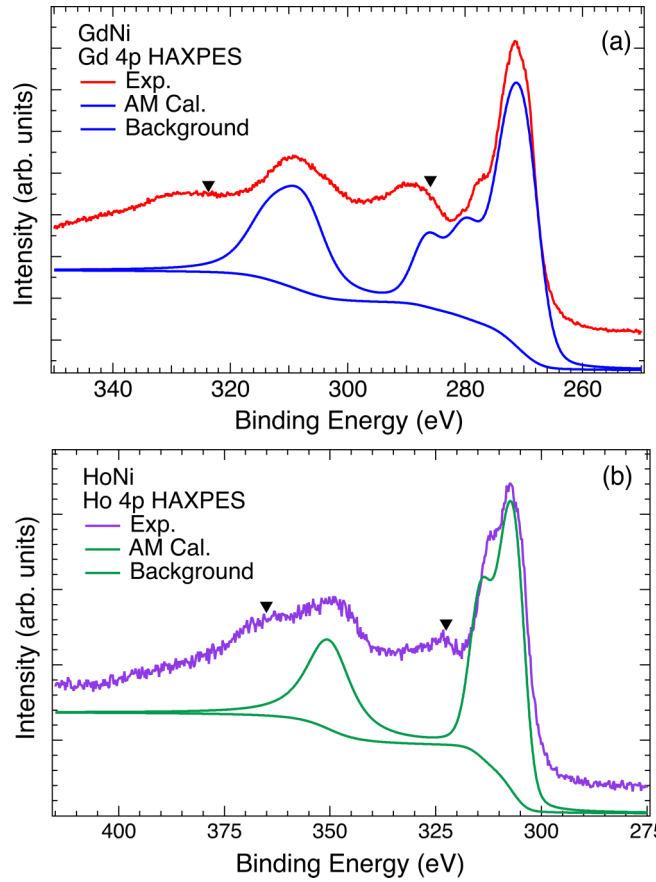

FIG. 6. (a) The Gd $4p$ HAXPES spectrum of GdNi measured at $T = 80$ K compared with atomic multiplet calculations. (b) The comparison of the Ho $4p$ HAXPES spectrum of HoNi measured at $T = 80$ K with atomic multiplet (AM) calculations.

the plasmon features; for completeness, the expected energy positions of the plasmon features are marked with inverted triangles corresponding to an energy separation of 14.6 eV from the highest-intensity main peak at BE of 271.5 eV and the feature at BE of 309.4 eV.

In Fig. 6(b), we plot the Ho $4p$ core-level spectrum of HoNi measured at $T = 80$ K. The spectrum shows a main peak at BE of 307.46 eV and a shoulder feature at a BE of 311.26 eV, followed by three weaker broad features at BEs of 322.66, 350.26, and 365.46 eV. We also carried out the atomic multiplet calculations for the Ho $4p$ spectrum, and the results are plotted in Fig. 6(b) along with the experiment. The calculated spectrum of HoNi shows several multiplet features spread in two energy ranges of BEs, between 305.5 and 317.1 eV and between 349.0 and 353.4 eV, resulting in a main peak at a BE of 307.46 eV, a shoulder feature at BE of 313.86 eV, and a broad feature at a higher BE of 350.96 eV. Also for the $4p$ spectrum of Ho, the CI effect is present because the binding energy of the $4p$ state is approximately twice that of the $4d$ state. Therefore, we assign the additional features in the experiment (and not seen in the multiplet calculations) at higher BEs of ∼322.66 and ∼365.46 eV mainly to this CI effect. The expected energy positions of the plasmon features overlap these features and are marked with inverted triangles, corresponding to an energy separation of 15.2 eV from the highest intensity main peak at BE of 311.26 eV and the feature at BE of 350.26 eV.

The Gd $5p$ core-level HAXPES spectrum of GdNi measured at $T = 80$ K is shown in Fig. 7(a). The spectrum consists of several peaks, with four narrower peaks at lower BEs of 20.19, 20.79, 21.59, and 22.71 eV, followed by two broad peaks at BEs of 24.89 and 27.16 eV. The shape of four narrow peaks at lower BE is quite similar to the shape of the Gd $3d$ and $4d$ spectra. The measured experimental spectrum is very consistent with the earlier studies on Gd metal thin films [43,47,48]. Atomic multiplet calculations for the Gd $5p$ spectrum are plotted in Fig. 7(a) along with the experiment. The overall experimental spectral features of Gd $5p$ are similar to the Gd $4d$ spectra. Thus, we use a similar analysis to describe the multiplets of Gd $5p$. From the jJ coupling scheme, the exchange interaction of $5p$ core-hole angular momentum $j = 3/2$ coupling with the $4f^7$ valence angular momentum $J = 7/2$ will split into four peaks with total angular momentum $J' = 5, 4, 3, 2$ at the lower BE side between 20 and 24 eV. Similarly, for $5p$ core-hole angular momentum $j = 1/2$ coupling with $J = 7/2$, it will result in two multiplet peaks $J' = 3, 4$, which are positioned at higher BEs between 24 and 29 eV. On the other hand, from the LS coupling scheme, the Gd $5p^5$ (^2D) states coupled with the $4f^7$ (^8S) state, resulting in the ^7P and ^9P states. The ^9P states occur at lower BE, while the ^7P states occur at higher BEs. If the spin-orbit coupling is small, the ^9P states and ^7P states will each split into three levels ($^9P_5$, $^9P_4$, $^9P_3$, $^7P_2$, $^7P_3$, $^7P_4$), but the ^7P states can also be formed by coupling with higher-energy terms ^6D and ^6F of the $4f^7$ states. Therefore, the Coulomb and exchange interaction between these ^7P states will not retain their original systematic pattern of jJ coupling. In our experimental results, the four narrow peaks at low BE are consistent with the jJ coupling scheme, but the two broad features at hight BE cannot be simply explained by the two

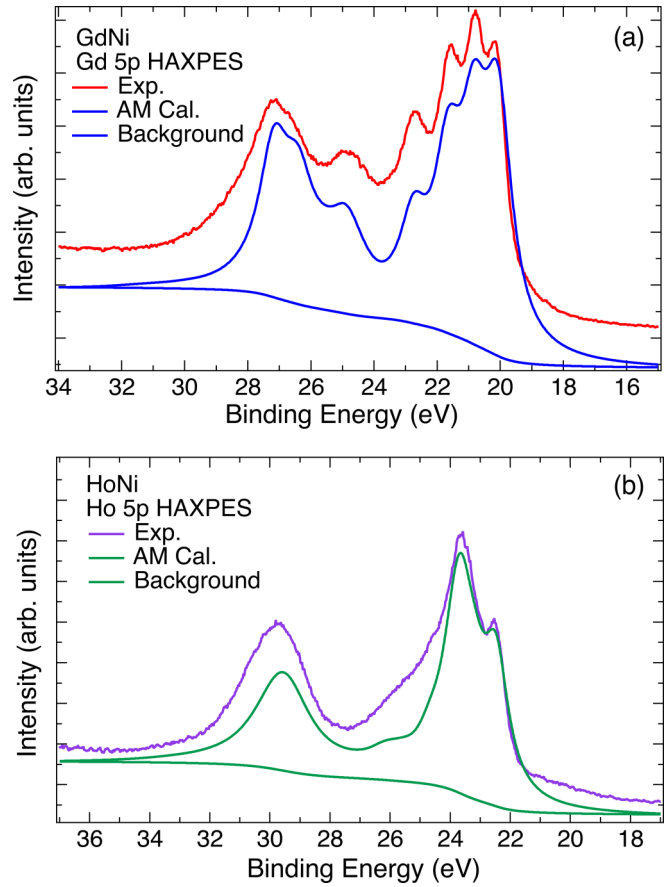

FIG. 7. (a) The Gd $5p$ HAXPES spectrum of GdNi measured at $T = 80$ K compared with atomic multiplet calculations. (b) The Ho $5p$ HAXPES spectrum of HoNi measured at $T = 80$ K compared with atomic multiplet (AM) calculations.

multiplet features $J' = 4, 3$ in the jJ coupling scheme. Since the width of the two peaks at high BE is broad, it is indicative of several peaks hidden inside the peaks. As was discussed for Gd metal, the mixing of higher-energy terms of the $4f^7$ configuration with low-spin ^7P states leads to a large lifetime broadening [43,48].

We also measured the Ho $5p$ core-level HAXPES spectrum of HoNi at $T = 80$ K as shown in Fig. 7(b). The spectrum has two broad peaks, and the lower BE broad peak consists of a small sharp feature at a BE of 22.54 eV and a high-intensity peak at a BE of 23.59 eV. The sharp feature at 22.54 eV was missing in earlier soft x-ray PES studies on $HoRhB_3$ [45] and HoB_4 [46], perhaps because of lower-energy resolution and surface sensitivity of soft x-ray PES compared to HAXPES. Another broad peak is positioned at a BE of 29.79 eV. It is interesting to note that the shape of the Ho $5p$ feature at lower BE is very similar to the shape of the Ho $3d$ spectrum at low BEs. The atomic multiplet calculations for the Ho $5p$ spectrum are plotted in Fig. 7(b), along with the experiment. We use a similar analysis as the Ho $4p$ spectrum to understand the atomic multiplets of the Ho $5p$ spectrum. From the jJ coupling scheme, we can obtain four multiplets with total angular momentum $J' = 19/2, 17/2, 15/2, 13/2$ at lower BE between 22 and 27 eV, and two multiplet peaks $J' = 17/2, 15/2$, at higher BEs between 28 and 32 eV. On the other hand,

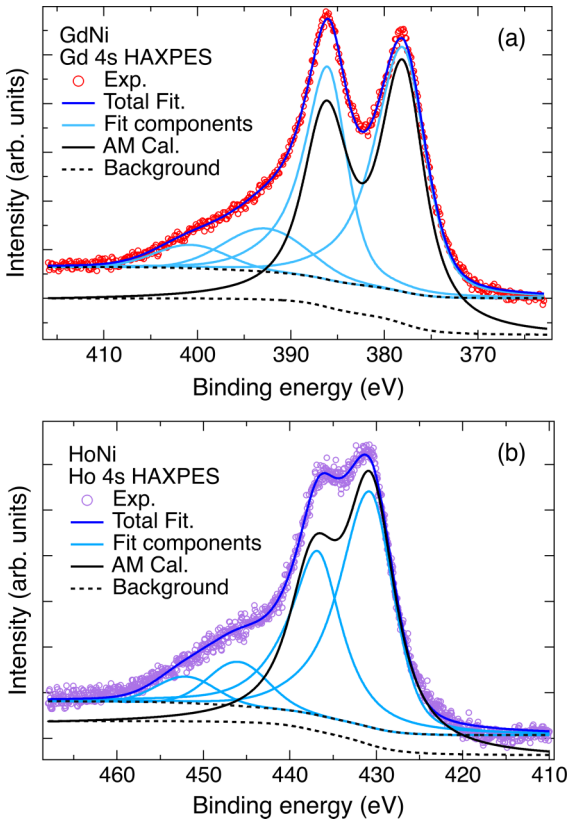

FIG. 8. (a) The Gd 4*s* HAXPES spectrum of GdNi measured at $T = 80$ K with fitting results obtained using a least-squares method. (b) The Ho 4*s* HAXPES spectrum of HoNi measured at $T = 80$ K compared with fitting results. The fitting parameters are listed in Table II. The black full lines in (a) and (b) show the atomic multiplet (AM) calculations.

from the *LS* coupling scheme, we obtain six final states: ^6K, ^6I, ^6H, ^4K, ^4I, ^4H, as in the Ho 4*p* case. Further, the ^6H, ^4K, ^4I, ^4H states can also be formed by coupling with the high-energy states (^5G, ^3G, ^3H, and ^3I) of Ho $4f^{10}(^5I)$. Thus, the *LS* terms at high BEs are mixed, and the Coulomb and exchange interaction between these mixed states will affect the energy position and intensities of these states. The regular pattern of *jJ* coupling is not expected to be retained, just as in Gd 4*d* and Gd 5*p* spectra, resulting in the ^4H states lying together with the ^6K, ^6I, and ^6H terms at the low BE side, and the ^4K, ^4I terms at the higher BE side.

In Figs. 8(a) and 8(b), we have plotted the Gd 4*s* and Ho 4*s* HAXPES spectra of GdNi and HoNi measured at $T = 80$ K. In general, a *Ns* (where *N* is the principal quantum number) core-level photoemission spectrum should be a single peak for materials without a local moment. But if the material has a local magnetic moment, then it will split the *Ns* level into two peaks due to the *Ns*-*Vm* interaction, where *Vm* is the local moment in the valence shell. As seen in our experimental spectra of Gd 4*s* and Ho 4*s*, both spectra show a clear two-peak structure with weaker satellites at higher BEs. The spectra are similar to that of the Gd and Ho metal spectra reported by Cohen *et al.* [50], and also to Gd containing binary alloys reported by Szade and Neumann [51]. In order to quantify the peaks, we have used a least-squares method

TABLE II. Fitting parameters for the Gd 4*s* and Ho 4*s* core-level spectra.

Fit component Gd 4*s*	Binding energy (eV)	FWHM (eV)
1	378.10	6.48
2	386.11	5.48
3	392.70	10.44
4	400.71	9.17
Ho 4*s*	(eV)	(eV)
1	430.80	7.36
2	436.84	7.10
3	446.00	8.00
4	452.04	8.00

to fit the 4*s* spectra of Gd and Ho in GdNi and HoNi. The fitting results are shown in Figs. 8(a) and 8(b), along with the experimental spectra, and the fitting parameters are listed in Table II. We first discuss the Gd 4*s* spectrum. The Gd 4*s* spectrum shows a doublet which is attributed to the 4*s*-4*f* exchange interaction. The 4*s* spin $s = 1/2$ up-spin and down-spin couples differently with the spin $S = 7/2$ in the $4f^7$ shell, resulting in a doublet with spin $S' = S \pm s$ corresponding to the ^9S and ^7S states. The ^9S is at the lower BE and the intensity ratio of ^9S and ^7S is expected to be proportional to the ratio of their multiplicities, i.e., $9/7 = 1.285$. In addition, the energy separation between the doublet is proportional to the 4*s*-4*f* exchange-interaction energy. In Fig. 8(a), the two satellite peaks are due to plasmon peaks corresponding to the Gd 4*s* doublet, as we know the plasmon energy in the Gd 4*d* core-level spectrum is ~14.6 eV from the other core-level spectra discussed above. The fitting data match well with the experiment. From the fitting results, we know that the energy separation of the Gd 4*s* doublet is 8.01 eV, the intensity ratio of the doublet is 1.30, and the full widths at half maximum (FWHM) are 6.48 and 5.48 eV, respectively. Our results for the energy separation match fairly well with earlier work [50,51]. In addition, the energy separation of 8.01 eV for the Gd 4*s* splitting is in good agreement with theoretical calculations of the Gd 4*s* exchange-interaction energy of ~8 eV obtained using the Slater model [50]. This confirms that the 4*s*-4*f* exchange interaction is larger than the *LS* coupling energy of the 4*f* electrons in the final states.

In Fig. 8(b), the Ho 4*s* HAXPES spectrum is plotted with the fitting results. Since we know that the plasmon energy is 15.2 eV from the Ho 3*d* and Ho 4*p* core-level spectra, we attribute the satellites in the Ho 4*s* spectra to the plasmon peaks positioned at 15.2 eV higher BE from the corresponding Ho 4*s* doublet. It is clear that the Ho 4*s* splitting is also due to the 4*s*-4*f* exchange interaction. From the fitting results, we know that the energy separation of the Ho 4*s* exchange splitting doublet is 6.04 eV. It is thus clear that the 4*s*-4*f* exchange splitting in GdNi (~8 eV) is larger than the exchange splitting in HoNi. The exchange splitting for Ho is consistent with the theoretical calculation obtained using the Slater model, which showed a value of 5.6 eV [50]. Further, while the FWHMs of the Ho 4*s* doublets are 7.36 and 7.10 eV, the intensity ratio of the Ho 4*s* doublet is 1.4. This is close to the ratio

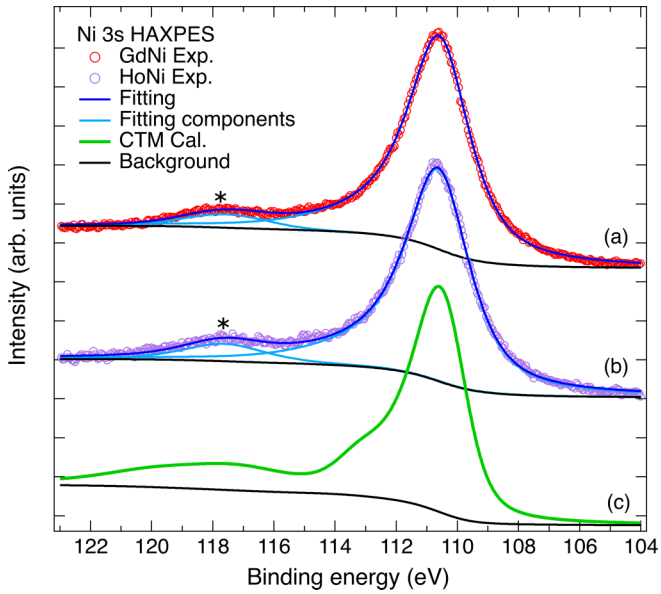

FIG. 9. (a) The Ni 3*s* HAXPES spectrum of GdNi measured at $T = 80$ K with fitting results obtained using a least-squares method. (b) The Ni 3*s* HAXPES spectrum of HoNi measured at $T = 80$ K compared with the fitting results. The fitting parameters are listed in Table III. (c) The calculated Ni 3*s* spectrum obtained using the charge transfer multiplet (CTM) model described in the text.

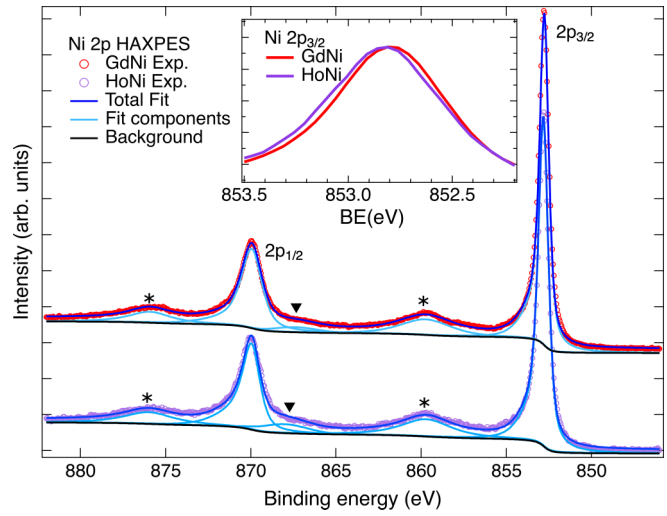

FIG. 10. The Ni 2*p* HAXPES spectra of GdNi and HoNi obtained at $T = 80$ K. The asterisk labels indicate the corresponding satellites of the $2p_{3/2}$ and $2p_{1/2}$ main peaks. The inverted triangles mark the weak plasmons. Inset: The $2p_{3/2}$ main peak of HoNi is shifted by a small value of about 50 meV to higher BE than GdNi.

of multiplicities, $6/4 = 1.5$, of the final doublet states ^6I and ^4I. We could reproduce the experimental 4*s* splitting and the observed ratio of the split peaks for GdNi and HoNi using atomic multiplet calculations. This is shown in Figs. 8(a) and 8(b) using black lines. While all the Hartree-Fock parameters were scaled to 80%, the value for the exchange-interaction parameter G^2_{sf} had to be reduced to 56% and 69% for Gd and Ho, respectively (see Table XV in the Appendix), in order to match the the 4*s* splitting in the atomic calculation with the experimental data.

The Ni 3*s* core-level HAXPES of GdNi and HoNi measured at $T = 80$ K are shown in Fig. 9. The Ni 3*s* spectrum of GdNi and HoNi are very similar, with both of them showing a high-intensity single peak around 111 eV and a small broad peak at higher BEs in both spectra. In order to quantitatively compare the Ni 3*s* spectra in GdNi and HoNi, we carried out a least-squares-method fitting of the experimental spectra. The fitting results are labeled (a) and (b) in Fig. 9, along with the experimental spectra. The fitting parameters are listed in Table III. We first discuss the Ni 3*s* spectrum of GdNi. The main peak of Ni 3*s* is positioned at a BE of 110.6 eV, and a small broad peak is positioned at a BE of 117.6 eV. The energy separation between these two peaks is 7 eV. For the Ni 3*s* spectrum in HoNi, the main peak of Ni 3*s* is positioned at BE of 110.63 eV and the small-feature broad peak is at BE of 117.63 eV, and hence for HoNi also, the energy separation between these two peaks is 7 eV. Surprisingly, this 7 eV energy separation also matches well with the energy separation between the main peak and satellite in the Ni 2*p* spectra discussed in Fig. 10. Thus, the satellite peaks are not plasmons in the Ni 3*s* spectra of GdNi and HoNi.

TABLE III. Fitting parameters for Ni 3*s* core-level spectra of GdNi and HoNi.

Fit component GdNi Ni 3*s*	Binding energy (eV)	FWHM (eV)
1	110.60	2.50
2	117.60	3.21
HoNi Ni3*s*	(eV)	(eV)
1	110.63	2.55
2	117.63	3.20

We have used the CTM program [36] to carry out model cluster calculations including atomic multiplets and charge transferred states. The initial and final states are a mixture of d^8 and $d^9\underline{L}^1$, where $\underline{L}^1$ represents a ligand hole state. A fair match of the calculated spectrum (labeled (c) in Fig. 9) with the experimental spectrum is obtained for the following parameters: charge transfer energy $\Delta = 1.5$ eV, on-site Coulomb energy $U_{dd} = 5.5$ eV, core-hole Coulomb attraction $U_{pd} = 6.5$ eV, crystal-field splitting $10\text{Dq} = -0.5$ eV, and hybridization strengths $V_{eg} = 2.18$ eV, $V_{t2g} = 1.45$ eV. It is noted that although the basic motif of the GdNi structure consists of a trigonal prism consisting of a Ni atom surrounded by six Gd ions, there are two additional Ni nearest-neighbor ions which results in a distorted cubic cluster of eight neighbors (six Gd ions and two Ni ions) surrounding the central Ni atom. The eightfold distorted cubic arrangement results in a negative 10Dq value, i.e., with an inversion of t_{2g} and e_g states. The Slater integrals were reduced to 0.48 compared to the Hartree-Fock values.

We then measured the Ni 2*p* HAXPES spectrum of GdNi and HoNi at $T = 80$ K, and the spectra are shown in Fig. 10. The spectrum of Ni 2*p* in GdNi and HoNi shows two high-intensity peaks, which are the $2p_{3/2}$ and $2p_{1/2}$ spin-orbit features. The spectra also show two small broad peaks at

TABLE IV. Fitting parameters for Ni $2p$ core-level spectra of GdNi and HoNi.

Fit component GdNi Ni $2p$	Binding energy (eV)	FWHM (eV)
$2p_{3/2}$ main	852.78	0.66
$2p_{3/2}$ satellite	859.72	3.50
Plasmon	867.38	3.00
$2p_{1/2}$ main	869.95	1.48
$2p_{1/2}$ satellite	875.93	2.98
HoNi Ni $2p$	(eV)	(eV)
$2p_{3/2}$ main	852.83	0.73
$2p_{3/2}$ satellite	859.70	3.50
Plasmon	868.03	3.20
$2p_{1/2}$ main	869.98	1.32
$2p_{1/2}$ satellite	876.00	3.50

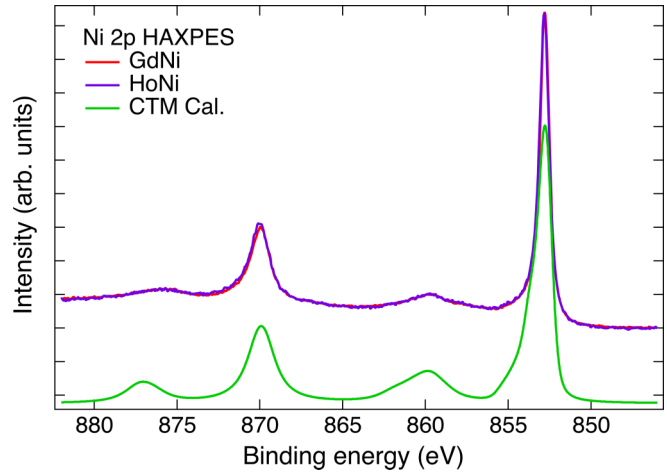

FIG. 11. The Ni $2p$ HAXPES spectra of GdNi and HoNi are compared with the charge transfer multiplet (CTM) calculations.

about 7 eV higher BEs compared to the main peaks. It is well known that the Ni $2p$ core-level spectrum of Ni metal shows a 6 eV correlation satellite feature [52,53]. The Ni $2p$ spectra of GdNi and HoNi are quite similar, but there are small differences between their spectral shapes, as shown in the expanded range of the $2p_{3/2}$ main peak in the inset in Fig. 10. In order to know the peak positions and widths, we did a least-squares fitting of the spectra. The fitting parameters are listed in Table IV and the fitting results are also plotted, together with the experiment in Fig. 10. In the beginning, we tried to use four peaks (two for the main peaks and two for the satellites) for the fitting. However, the fits always showed some discrepancy at BEs just below the $2p_{1/2}$ main peak. The energy position suggested that it could be associated with a weak plasmon contribution which is not easily visible to the eye. Thus, we included Gaussian-type plasmon peaks in the Ni $2p$ fitting and the fitting results showed a good match with the experiment.

For the Ni $2p$ spectrum of GdNi, the $2p_{3/2}$ main peak is positioned at BE of 852.78 eV, the corresponding satellite is positioned at BE of 859.72 eV, and the energy separation between the $2p_{3/2}$ main peak and satellite is 6.94 eV. On the other hand, the $2p_{1/2}$ main peak is at BE of 869.95 eV and the satellite of $2p_{1/2}$ is at BE of 875.93 eV, indicating an energy separation of 5.98 eV. The plasmon peak is positioned at BE of 867.38 eV, which is 14.6 eV higher BE than the $2p_{3/2}$ peak. For the Ni $2p$ HAXPES spectrum of HoNi, the position of the Ni $2p_{3/2}$ main peak is at BE of 852.83 eV, the corresponding satellite is at BE of 859.7 eV, and the energy separation between the main peak and satellite of $2p_{3/2}$ is 6.87 eV. Similarly, the $2p_{1/2}$ main peak is at a BE of 869.98 eV and the $2p_{1/2}$ satellite is at 6.02 eV higher BE than the main peak. The plasmon peak is at BE of 868.03 eV, which is 15.2 eV higher BE than the main peak of $2p_{3/2}$. A careful look at the Ni $2p_{3/2}$ main peak spectra of GdNi and HoNi shows that the main peak of HoNi is positioned about 50 meV higher BE than that of GdNi, as shown in the inset in Fig. 10. This indicates that there is a small difference between GdNi and HoNi. The small difference suggests that the Ni ions receive a little more electronic charge from Gd nearest neighbors in GdNi, compared to the Ni ions in HoNi, perhaps due to the crystal structure difference between them. On the other hand, the energy separation between the main peak and satellite of $2p_{3/2}$ in GdNi and HoNi (∼7 eV) is larger than the 6 eV energy separation in Ni metal. Similarly, the energy separation between the main peak and the satellites of $2p_{1/2}$ in GdNi and HoNi (∼6 eV) is also larger than the 4.6 eV energy separation in Ni metal. This indicates that the electronic parameters for describing the Ni states in HoNi and GdNi are modified compared to Ni metal.

We carried out model cluster calculations for the Ni $2p$ spectra and the results are shown in Fig. 11 along with the experimental spectra. The same electronic parameters as for the Ni $3s$ calculated spectrum was used to calculate the Ni $2p$ spectrum. The small discrepancies between the experiment and calculation are attributed to the fact that we have used just two basis states in our calculations and additional screening channels are required to get a better match, as shown recently for transition-metal compounds [54]. The d-electron count is obtained to be 8.33 and this is significantly lower than the d-electron count of ∼9–9.2 known for Ni metal [52,55].

In Fig. 12, we compare the valence band of HoNi and GdNi measured at $T = 80$ K. The valence band of GdNi was recently reported by us [11], but we discuss it here for completeness to make a detailed comparison with HoNi. It was shown that the Gd $4f$ states occur at a BE of 8 eV, and the Ni $3d$ density of states (DOS) were observed between 0 and ∼3.5 eV BE, with a high-intensity sharp peak at E_F. The Ni $3d$ feature at E_F indicates that the Ni $3d$ band is partially occupied and invalidates the charge transfer model for GdNi [11]. This assignment is qualitatively consistent with band structure calculations of the Ni $3d$ density of states obtained using a tight-binding linear muffin-tin orbitals (TB-LMTO) method [56], but the high-intensity Ni $3d$ peak occurs at about 1.3 eV BE in the calculations. Further, the Gd $4f$ occupied states occur at about 4.8 eV BE in the calculations with weak contribution from Gd $5d$ states between the Fermi level and 5 eV BE. Hence, we cannot rule out Gd $5d$ contributions to the features assigned to the Ni $3d$ states. It is noted that soft x-ray photoemission studies on several Gd-based intermetallics [57–62] containing Gd and Ni, such as

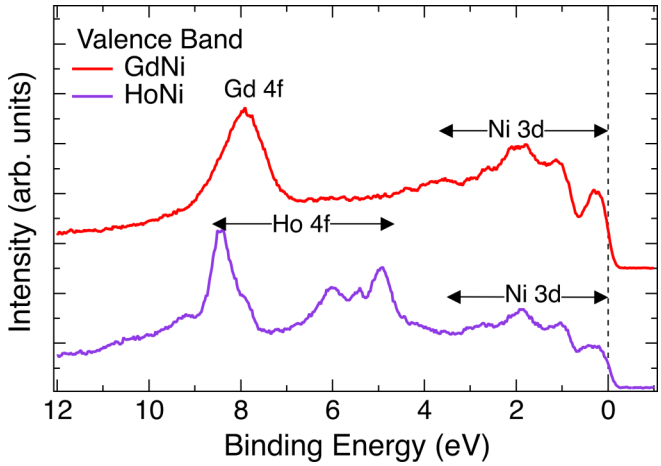

FIG. 12. The valence band of HoNi and GdNi measured at $T = 80$ K. The Ni $3d$ DOS at BE is observed within 3 eV from E_F for GdNi and HoNi, while the Gd $4f$ states are at 8 eV BE away from E_F, and the Ho $4f$ states are spread from 4 to 9 eV BE. The dashed line is E_F. The GdNi spectrum is taken from Ref. [11].

$GdNi_{5-x}Al_x$, Gd_3Ni_8Al, $GdNi_4B$, $GdNi_4Si$, $Gd(Ni_{1-x}Co_x)_3$, $Gd(Ni_{1-x}Fe_x)_3$, and Gd_3Ni, have shown a broad Gd $4f$ derived feature at 8 eV BE, while the Ni $3d$ states occur between the Fermi level and about 3.5 eV BE.

On the other hand, the valence band of HoNi shows Ho $4f$ DOS consisting of several features spread between 4 and 9 eV BE, while the Ni $3d$ DOS still occurs between 0 and ~3.5 eV BE. The Ni $3d$ spectral features and BE positions are quite similar to Ni $3d$ states in GdNi. This indicates that the Ni $3d$ band is partially occupied even in HoNi, making it inconsistent with the charge transfer model. However, one important difference is that the feature at E_F is broader and shows lower relative intensity compared to GdNi, when the main $4f$ features of GdNi and HoNi are normalized, as shown in Fig. 12. This normalization is roughly consistent with the relative f-electron occupancies of f^7:f^{10} for GdNi and HoNi as estimated from the $4f$ features after a background subtraction, respectively. This suggests that the number of carriers at the Fermi level is lower in HoNi compared to GdNi, but not an order-of-magnitude smaller as implied by the specific heat γ estimated for HoNi compared to GdNi [18,19]. The Ho $4f$ features are very consistent with the valence-band PES spectrum of Ho metal, which were analyzed in terms of an intermediate-coupling scheme by Thole and van der Laan [63]. The highest-intensity peak at 8.5 eV BE consists of the ^4F, ^4G, ^4M, ^4K, ^4I, while the feature at 5 eV BE is mainly due to $^6H_{15/2}$ states. The remaining Ho $4f$ feature at 6 eV BE is due to ^6F final states. Qualitatively similar Ho $4f$ features are also observed in the Ho compounds $HoRhB_3$ [45], HoB_4 [46], and $HoNi_4B$ [64].

For GdNi, the 8 eV BE broad peak of the Gd $4f$ states is assigned to ^7F states consisting of seven closely spaced multiplets, which make one smooth broad feature. Since the Ni $3d$ lowest BE feature cuts the E_F level in HoNi and GdNi, it indicates a partially filled Ni $3d$ band in HoNi, just like in GdNi. Since GdNi is ferrimagnetic with a small finite Ni magnetic moment, and since HoNi is considered ferromagnetic, the present result suggests that it would be important to investigate the Ni moment in HoNi using XMCD studies. It may be expected to show a small finite magnetic moment, which is likely antiferromagnetically coupled to the large magnetic momentum of Ho ($\sim 9.2\,\mu_B$). In a recent study, it was discussed that the Ni $3d$ states would participate in charge and thermal transport processes. However, the very small magnetic moment of Ni in GdNi suggests it would result in a weak contribution to the magnetocaloric effect, while the large Gd spin moments would play a dominant role in the magnetocaloric properties of GdNi. We expect a similar picture to be valid for the HoNi with relatively lower Ni $3d$ density of states at the Fermi level, and a larger Ho total magnetic moment, resulting in a comparable magnetoresistance to GdNi as is known from experiment [34,35].

Finally, it is important to note that the atomic multiplet calculations matched fairly well with the experimental $3d$, $4d$, $4p$, $5p$, and $4s$ core-level spectra of GdNi and HoNi. This is in contrast to the core-level spectra of transition-metal compounds as well as early lanthanide (La to Sm) intermetallic alloys [8,38,65], which always show charge transfer satellites in experiments. The charge transfer satellites in the experimental spectra can be reproduced in calculations only if ligand screened configurations are taken into account. In fact, even for the Ni $3s$ and Ni $2p$ spectra, we see satellites in GdNi and HoNi which can be explained only by including ligand screened configurations, as shown in Figs. 9 and 11. The reason that ligand screened states are not required for the late lanthanides (Eu to Lu) is based on the fact that the hybridization strength for the late lanthanides with nearest-neighbor ligands is very small, as shown from $3d$ core-level photoemission spectroscopy experiments of the lanthanides [65] and consistent with the lanthanide contraction in the series [66]. It would be interesting to carry out HAXPES core-level experiments on an isostructural series spanning across the full lanthanide series to see the evolution of their electronic structure parameters.

IV. CONCLUSIONS

In conclusion, the electronic structure of GdNi and HoNi was investigated using HAXPES combined with atomic multiplet calculations for Gd^{3+} and Ho^{3+} configurations. The results show that both GdNi and HoNi core-level spectra are best explained by the intermediate-coupling scheme. The analysis of the Gd and Ho $4s$ spectra show the exchange interaction between the $4s$-$4f$ states to be stronger in GdNi compared to HoNi. The Ni $2p$ and $3s$ spectra show correlation satellites which indicate that the Ni $3d$ states in GdNi and HoNi are more correlated than in Ni metal. Valence-band HAXPES of GdNi and HoNi shows that the Gd $4f$ and Ho $4f$ features are localized and occur at high binding energies away from the Fermi level. The Ni $3d$ DOS are positioned at and near the Fermi level, indicating a partially filled Ni $3d$ band in GdNi and HoNi. The results establish that the charge transfer model, which predicts a fully filled Ni $3d$ band, is not valid for describing the electronic structure of GdNi and HoNi.

ACKNOWLEDGMENTS

A.C. thanks the Ministry of Science and Technology (MOST) of Taiwan, Republic of China, for financially supporting this research under Contract No. MOST 108-2112-M-213-001-MY3. D.M. and A.C. thank the France-Taiwan (CNRS-MOST) bilateral project for financially supporting this research under Contract No. CNRS 290771 and Contract No. MOST 108-2911-I-213-501, respectively.

APPENDIX

Tables V–XV list the electronic parameters used in the atomic multiplet calculations and Tables XVI–XIX list the electronic parameters used in the charge transfer multiplet calculations.

TABLE V. Gd and Ho 3*d*, 4*d*, 4*p*, 5*p*, 4*s* Hartree-Fock (HF) parameter values in the initial state.

HF value (eV)	Gd	Ho
F^2_{ff}	14.502	15.7059
F^4_{ff}	9.1012	9.8538
F^6_{ff}	6.5482	7.089
ζ_{4f}	0.1973	0.2734

TABLE VI. Gd and Ho 3*d* Hartree-Fock reduction factor (RF) values in the initial state.

RF	Gd	Ho
F^2_{ff}	0.85	0.80
F^4_{ff}	0.85	0.80
F^6_{ff}	0.85	0.80
ζ_{4f}	0.98	0.99

TABLE VII. Gd and Ho 3*d* HF and RF values in the final state.

HF value (eV)	Gd	RF	Ho	RF
F^2_{ff}	15.1948	0.9	16.3422	0.9
F^4_{ff}	9.5496	0.9	10.265	0.9
F^6_{ff}	6.8748	0.9	7.3883	0.9
F^2_{df}	9.7125	0.9	10.7163	0.9
F^4_{df}	4.5316	0.9	5.0507	0.9
G^1_{df}	6.9463	0.9	7.7995	0.85
G^3_{df}	4.0725	0.9	4.576	0.85
G^5_{df}	2.8134	0.9	3.1622	0.85
ζ_{4f}	0.2255	0.98	0.3067	0.99
ζ_{3d4f}	12.3581	0.98	15.5763	0.99

TABLE VIII. Gd and Ho 4*d* RF values in the initial state.

RF	Gd	Ho
F^2_{ff}	0.85	0.85
F^4_{ff}	0.85	0.85
F^6_{ff}	0.85	0.85
ζ_{4f}	1.0	1.0

TABLE IX. Gd and Ho 4*d* HF and RF values in the final state.

HF value (eV)	Gd	RF	Ho	RF
F^2_{ff}	14.6635	0.9	15.8434	0.85
F^4_{ff}	9.209	0.9	9.9455	0.85
F^6_{ff}	6.6276	0.9	7.1565	0.85
F^2_{df}	16.4158	0.75	17.6626	0.98
F^4_{df}	10.4946	0.75	11.2902	0.98
G^1_{df}	19.3646	0.77	20.7696	0.78
G^3_{df}	12.166	0.85	13.0727	0.78
G^5_{df}	8.6049	0.85	9.2521	0.78
ζ_{4f}	0.2013	1.0	0.2775	1.0
ζ_{4d}	2.1905	1.0	2.8146	1.0

TABLE X. Gd and Ho 4*p* RF values in the initial state.

RF	Gd	Ho
F^2_{ff}	0.7	0.7
F^4_{ff}	0.7	0.7
F^6_{ff}	0.7	0.7
ζ_{4f}	1.0	0.96

TABLE XI. Gd and Ho 4*p* HF and RF values in the final state.

HF value (eV)	Gd	RF	Ho	RF
F^2_{ff}	14.7868	0.7	15.9532	0.7
F^4_{ff}	9.292	0.7	10.0196	0.7
F^6_{ff}	6.689	0.7	7.2113	0.7
F^2_{df}	17.1125	0.7	18.4124	0.7
G^2_{pf}	14.8385	0.95	15.938	0.7
G^4_{pf}	10.2388	0.95	11.0148	0.7
ζ_{4f}	0.2038	1.0	0.2802	0.96
ζ_{4p}	21.2048	1.0	27.0028	0.96

TABLE XII. Gd and Ho 5*p* RF values in the initial state.

RF	Gd	Ho
F^2_{ff}	0.8	0.8
F^4_{ff}	0.8	0.8
F^6_{ff}	0.8	0.85
ζ_{4f}	1.0	1.0

TABLE XIII. Gd and Ho 5*p* HF and RF values in the final state.

HF value (eV)	Gd	RF	Ho	RF
F^2_{ff}	14.787	0.8	15.9601	0.8
F^4_{ff}	9.295	0.8	10.0271	0.8
F^6_{ff}	6.692	0.8	7.2171	0.8
F^2_{df}	6.788	0.8	6.9823	0.8
G^2_{pf}	3.408	0.85	3.4394	0.8
G^4_{pf}	2.666	0.85	2.6934	0.8
ζ_{4f}	0.201	1.0	0.2772	1.0
ζ_{4p}	2.974	1.0	3.6492	1.0

TABLE XIV. Gd and Ho 4*s* RF values in the initial state.

RF	Gd	Ho
F^2_{ff}	0.8	0.8
F^4_{ff}	0.8	0.8
F^6_{ff}	0.8	0.8
ζ_{4f}	1.0	1.0

TABLE XV. Gd and Ho 4*s* HF and RF values in the final state.

HF value (eV)	Gd	RF	Ho	RF
F^2_{ff}	15.721	0.8	16.847	0.8
F^4_{ff}	9.927	0.8	10.627	0.8
F^6_{ff}	7.16	0.8	7.662	0.8
G^2_{sf}	12.747	0.563	13.649	0.69
ζ_{4f}	0.22	1.0	0.299	1.0
ζ_{4s}	0.185	1.0	0.214	1.0

TABLE XVI. Ni 2*p* and Ni 3*s* HF and RF values in the initial state.

HF value (eV)	$3d^8$	$3d^9\underline{L}$	RF
F^2_{dd}	15.291		0.48
F^4_{dd}	9.498		0.48
ζ_{3d}	0.083	0.074	1.0

TABLE XVII. Ni 2*p* HF and RF values in the final state.

HF value (eV)	$2p^53d^9$	$2p^53d^{10}\underline{L}$	RF
F^2_{pd}	10.437	9.652	0.48
G^1_{pd}	7.915	7.235	0.4
G^3_{pd}	4.505	4.115	0.4
ζ_{3d}	0.112	0.102	1.0
ζ_{2p}	11.506	11.507	0.958

TABLE XVIII. Ni 3*s* HF and RF values in the final state.

HF value (eV)	$3s^13d^9$	$3s^13d^{10}\underline{L}$	RF
G^1_{sd}	12.785	11.933	0.48
ζ_{3d}	0.093	0.085	1.0

TABLE XIX. Ni 2*p* and 3*s* charge transfer multiplet calculation parameters in eV.

	U_{dd}	U_{pd}	10Dq	Δ	V_{eg}	V_{t2g}
Ni 2*p*, Ni 3*s*	5.5	6.5	−0.5	1.5	2.18	1.45

[1] A. M. Tishin and Y. I. Spichkin, *The Magnetocaloric Effect and its Applications* (Institute of Physics Publishing, Bristol, 2003).

[2] K. A. Gschneidner, Jr., V. K. Pecharsky, and A. O. Tsokol, Recent developments in magnetocaloric materials, Rep. Prog. Phys. **68**, 1479 (2005).

[3] S. B. Roy, Magnetocaloric effect in intermetallic compounds and alloys, in *Handbook of Magnetic Materials*, edited by K. H. J. Buschow (North-Holland, Amsterdam, 2014), Vol. 22, Chap. 2, pp. 203–316.

[4] V. Franco, J. S. Blazquez, J. J. Ipus, J. Y. Law, L. M. Moreno-Ramirez and A. Conde, Magnetocaloric effect: From materials research to refrigeration devices, Prog. Mater. Sci. **93**, 112 (2018).

[5] K. N. R. Taylor, Intermetallic rare-earth compounds, Adv. Phys. **20**, 603 (1971).

[6] W. E. Wallace, *Rare Earth Intermetallics* (Academic, New York, 1973).

[7] K. H. J. Buschow, Rare earth compounds, in *Handbook of Ferromagnetic Materials*, edited by W. P. Wohlfarth (North-Holland, Amsterdam, 1980), Vol. 1, Chap. 4, pp. 297–414.

[8] M. Imada, A. Fujimori, and Y. Tokura, Metal-insulator transitions, Rev. Mod. Phys. **70**, 1039 (1998).

[9] R. C. Taylor, Magnetic properties of amorphous GdFe films prepared by evaporation, J. Appl. Phys. **47**, 1164 (1976).

[10] K. Yano, I. Umehara, K. Sato, and A. Yaresko, Revelation of Ni magnetic moment in GdNi single crystal by soft x-ray magnetic circular dichroism, Solid State Commun. **136**, 67 (2005).

[11] C. W. Chuang, H. J. Lin, F. M. F. de Groot, F. H. Chang, C. T. Chen, Y. Y. Chin, Y. F. Liao, K. D. Tsuei, J. Arout Chelvane, R. Nirmala, and A. Chainani, Electronic structure investigation of GdNi using x-ray absorption, magnetic circular dichroism and hard x-ray photoemission spectroscopy, Phys. Rev. B **101**, 115137 (2020).

[12] M. Mizumaki, K. Yano, I. Umehara, F. Ishikawa, K. Sato, A. Koizumi, N. Sakai, and T. Muro, Verification of Ni magnetic moment in $GdNi_2$ Laves phase by magnetic circular dichroism measurement, Phys. Rev. B **67**, 132404 (2003).

[13] R. E. Walline and W. E. Wallace, Magnetic and structural characteristics of lanthanide-nickel compounds, J. Chem. Phys. **41**, 1587 (1964).

[14] S. C. Abrahams, J. L. Bernstein, R. C. Sherwood, J. H. Wernick, and H. J. Williams, The crystal structure and magnetic properties of the rare-earth nickel (RNi) compounds, J. Phys. Chem. Solids **25**, 1069 (1964).

[15] D. Gignoux and J. C. Gomez-Sal, Magnetic properties and structures of the rare earth compounds $RNi_{1-x}Cu_x$ with the FeB-type structure, J. Magn. Magn. Mater. **1**, 203 (1976).

[16] K. Mori and K. Sato, Temperature Dependence of Electrical Resistivity in Ferromagnetic GdNi Single Crystal, J. Phys. Soc. Jpn. **49**, 246 (1980).

[17] K. Sato, Y. Isikawa, and K. Mori, Magnetization and electrical resistivity studies of the HoNi single crystal, J. Appl. Phys. **53**, 8222 (1982).

[18] K. Sato, Y. Isikawa, K. Mori, and T. Miyazaki, Specific heat of ferromagnetic compounds RNi, J. Appl. Phys. **67**, 5300 (1990).

[19] I. Umehara, M. Endo, A. Matsuda, S. Fujimori, Y. Adachi, Y. Isikawa, and K. Sato, Crystalline electric field effect in single crystalline HoNi, J. Magn. Magn. Mater. **177**, 1143 (1998).

[20] I. Ursu and E. Burzo, Paramagnetic resonance of the gadolinium-nickel intermetallic compounds, J. Magn. Resonance **8**, 274 (1972)

[21] C. A. Poldy and K. N. R. Taylor, A possible influence of 3*d* states on the stability of rare earth-rich rare earth-transition metal compounds, Phys. Stat. Solidi A **18**, 123 (1973).

[22] R. Mallik, P. L. Paulose, E. V. Sampathkumaran, S. Patil, and V. Nagarajan, Coexistence of localized and (induced) itinerant magnetism and heat-capacity anomaliesin $Gd_{1-x}Y_xNi$ alloys, Phys. Rev. B **55**, 8369 (1997).

[23] D. Paudyal, Ya. Mudryk, Y. B. Lee, V. K. Pecharsky, K. A. Gschneidner, Jr., and B. N. Harmon, Understanding the extraordinary magnetoelastic behavior in GdNi, Phys. Rev. B **78**, 184436 (2008).

[24] J. A. Blanco, J. C. Gomez Sal, J. R. Fernandez, D. Gignoux, D. Schmitt, and J. R. Carvajal, Magnetic and electrical properties of $GdNi_{1-x}Cu_x$ compounds, J. Phys. Condens. Matter **4**, 8233 (1992).

[25] D. Gignoux and J. S. Shah, Magnetic structure of the compound DyNi, Solid State Commun. **11**, 1709 (1972).

[26] Y. Isikawa, K. Mori, K. Sato, M. Ohashi, and Y. Yamaguchi, Neutron diffraction measurement and the magnetic structure of the HoNi compound, J. Appl. Phys. **55**, 2031 (1984).

[27] J. A. Blanco, J. R. Fernandez, J. C. Gomez Sal, J. R. Carvajal and D. Gignoux, Magnetic properties and magnetic structures of $Ho_{1-x}Y_xNi$ compounds, J. Phys.: Condens. Matter **7**, 2843 (1995).

[28] X.-Q. Zheng and B.-G. Shen, The magnetic properties and magnetocaloric effects in binary $R-T$ (R = Pr, Gd, Tb, Dy, Ho, Er, Tm; T = Ga, Ni, Co, Cu) intermetallic compounds, Chin. Phys. B **26**, 027501 (2017).

[29] C. S. Fadley, Hard X-ray photoemission with angular resolution and standing-wave excitation, J. Electron Spectrosc. Relat. Phenom. **190**, 165 (2013).

[30] *Hard X-ray Photoelectron Spectroscopy (HAXPES)*, edited by J. C. Woicik (Springer International, Switzerland, 2016), Vol. 59.

[31] M. W. Haverkort, M. Zwierzycki, and O. K. Andersen, Multiplet ligand-field theory using Wannier orbitals, Phys. Rev. B **85**, 165113 (2012).

[32] Y. Lu, M. Hoppner, O. Gunnarsson, and M. W. Haverkort, Efficient real-frequency solver for dynamical mean-field theory, Phys. Rev. B **90**, 085102 (2014).

[33] M. Haverkort, G. Sangiovanni, P. Hansmann, A. Toschi, Y. Lu, and S. Macke, Bands, resonances, edge singularities and excitons in core level spectroscopy investigated within the dynamical mean-field theory, Europhys. Lett. **108**, 57004 (2014).

[34] P. Kumar, K. G. Suresh, A. K. Nigam, and O. Gutfleisch, Large reversible magnetocaloric effect in RNi compounds, J. Phys. D: Appl. Phys. **41**, 245006 (2008).

[35] R. Rajivgandhi, J. Arout Chelvane, S. Quezado, S. K. Malik, and R. Nirmala, Effect of rapid quenching on the magnetism and magnetocaloric effect of equiatomic rare earth intermetallic compounds *R*Ni (*R*= Gd, Tb and Ho), J. Magn. Magn. Mater. **433**, 169 (2017).

[36] E. Stavitski and F. M. F. de Groot, The CTM4XAS program for EELS and XAS spectral shape analysis of transition metal L edges, Micron **41**, 687 (2010).

[37] F. M. F. de Groot, Multiplet effects in x-ray spectroscopy, Coord. Chem. Rev. **249**, 31 (2005).

[38] F. M. F. de Groot and A. Kotani, *Core Level Spectroscopy of Solids* (CRC Press, Boca Raton, FL, 2008).

[39] H. J. Elmers, A. Chernenkaya, K. Medjanik, M. Emmel, G. Jakob, G. Schnhense, D. Gottlob, I. Krug, F. M. F. de Groot, and A. Gloskovskii, Exchange coupling in the correlated electronic states of amorphous GdFe films, Phys. Rev. B **88**, 174407 (2013).

[40] S. P. Kowalczyk, N. Edelstein, F. R. McFeely, L. Ley and D. A. Shirley, X-ray photoemission spectra of the 4*d* levels in rare-earth metals, Chem. Phys. Lett. **29**, 491 (1974)

[41] H. Ogasawara, A. Kotani, and B. T. Thole, Lifetime effect on the multiplet structure of 4*d* x-ray-photoemission spectra in heavy rare-earth elements, Phys. Rev. B **50**, 12332 (1994).

[42] G. van der Laan, E. Arenholz, E. Navas, A. Bauer, and G. Kaindl, Magnetic circular dichroism and orbital momentum coupling in 4*d* photoemission from Gd(0001), Phys. Rev. B **53**, R5998(R) (1996).

[43] W. J. Lademan, A. K. See, and L. E. Klebanoff and G. van der Laan, Multiplet structure in high-resolution and spin-resolved x-ray photoemission from gadolinium, Phys. Rev. B **54**, 17191 (1996).

[44] J. Szade, M. Neumann, I. Karla, B. Schneider, F. Fangmeyer, and M. Matteucci, Photon energy dependence of the Gd 4*d* photoemission, Solid State Commun. **113**, 709 (2000).

[45] T. Shishido, M. Oku, T. Sasaki, H. Iwasaki, H. Kishi, H. Horiuchi, and T. Fukuda, XPS and magnetic measurements for perovskite-type $HoRhB_3$, J. Alloys Compd. **283**, 91 (1999).

[46] D. Biswas, N. Sahadev, G. Adhikary, G. Balakrishnan, and K. Maiti, Evolution of the electronic structure of HoB_4 with temperature, Phys. Rev. B **88**, 134405 (2013).

[47] B. T. Thole, X. D. Wang, B. N. Harmon, Dongqi Li, and P. A. Dowben, Multiplet fine structure in the photoemission of the gadolinium and terbium 5*p* levels, Phys. Rev. B **47**, 9098 (1993).

[48] G. van der Laan, E. Arenholz, E. Navas, Z. Hu, E. Mentz, A. Bauer, and G. Kaindl, Magnetic circular dichroism in 5*p* photoemission from Gd and Tb metal, Phys. Rev. B **56**, 3244 (1997).

[49] A. Tagliaferri, L. Braicovich, G. van der Laan, G. Ghiringhelli, N. B. Brookes, C. Dallera, M. Finazzi, E. Weschke, Z. Hu, and G. Kaindl, Phys. Rev. B **60**, 5728 (1999).

[50] R. L. Cohen, G. K. Wertheim, A. Rosencwaig, and H. J. Guggenheim, Multiplet Splitting of the 4*s* and 5*s* Electrons of the Rare Earths, Phys. Rev. B **5**, 1037 (1972).

[51] J. Szade, M. Neumann, Photoelectron spectroscopy and magnetism of some gadolinium intermetallic compounds, J. Alloys Compd. **236**, 132 (1996).

[52] G. van der Laan and B. T. Thole, Electronic correlations in Ni $2p$ and $3p$ magnetic x-ray dichroism and x-ray photoemission of ferromagnetic nickel, J. Phys.: Condens. Matter **4**, 4181 (1992).

[53] O. Karis, S. Svensson, J. Rusz, P. M. Oppeneer, M. Gorgoi, F. Schafers, W. Braun, W. Eberhardt, and N. Martensson, High-kinetic-energy photoemission spectroscopy of Ni at $1s$: 6-eV satellite at 4 eV, Phys. Rev. B **78**, 233105 (2008).

[54] Mahnaz Ghiasi, Atsushi Hariki, Mathias Winder, Jan Kunes, Anna Regoutz, Tien-Lin Lee, Yongfeng Hu, Jean-Pascal Rueff, and Frank M. F. de Groot, Charge-transfer effect in hard x-ray $1s$ and $2p$ photoemission spectra: LDA+DMFT and cluster-model analysis, Phys. Rev. B **100**, 075146 (2019).

[55] T. Jo and G. A. Sawatzky, Ground state of ferromagnetic nickel and magnetic circular dichroism in Ni 2p core x-ray-absorption spectroscopy, Phys. Rev. B **43**, 8771(R) (1991).

[56] J. Rusz, I. Turek, and M. Divis, Random-phase approximation for critical temperatures of collinear magnets with multiple sublattices: GdX compounds (X = Mg, Rh, Ni, Pd), Phys. Rev. B **71**, 174408 (2005).

[57] E. Talik and M. Neumann, XPS investigations of Y_3Ni and Gd_3Ni single crystals, Physica B **193**, 207 (1994).

[58] M. Coldea, S. G. Chiuzbaian, M. Neumann, D. Todoran, M. Demeter, R. Tetean, and V. Pop, Magnetic and electronic properties of $GdNi_{5-x}Al_x$ intermetallic compounds, Acta Phys. Pol. A **98**, 629 (2000).

[59] V. Pop, M. Coldea, M. Neumann, S. Chiuzbaian, and D. Todoran, X-ray photoelectron spectroscopy and magnetism of Gd_3Ni_8Al, J. Alloys Compd. **333**, 1 (2002).

[60] A. Kowalczyk, A. Szajek, M. Falkowski, and G. Chełkowska, Magnetic properties and electronic structure of $GdNi_4Si$ compound, J. Magn. Magn. Mater. **305**, 348 (2006).

[61] M. Kwiecień, G. Chełkowska, and K. Rabijasz, Electronic structure, magnetic and electric properties of $Gd(Ni_{1-x}Co_x)_3$ compounds, J. Alloys Compd. **423**, 55 (2006).

[62] A. Bajorek, A. Chrobak, G. Chełkowska, and M. Kwiecień, Influence of Fe substitution on the structure and magnetic properties in $Gd(Ni_{1-x}Fe_x)_3$ intermetallic compounds, J. Alloys Compd. **485**, 6 (2009).

[63] B. T. Thole and G. van der Laan, Sum Rules for Magnetic Dichroism in Rare Earth $4f$ Photoemission, Phys. Rev. Lett. **70**, 2499 (1993).

[64] M. Pugaczowa-Michalska, T. Toliński, A. Kowalczyk, and G. Chełkowska, Properties of $HoNi_4B$ compound: X-ray photoemission and electronic structure, Czech. J. Phys. **54**, 347 (2004).

[65] F. U. Hillebrecht and J. C. Fuggle, Invalidity of $4f$ count determination and possibilities for determination of $4f$ hybridization in intermetallics of the light rare earths by core level spectroscopy, Phys. Rev. B **25**, 3550 (1982).

[66] D. van der Marel and G. A. Sawatzky, Electron-electron interaction and localization in d and f transition metals, Phys. Rev. B **37**, 10674 (1988).